J. Coat. Technol. Res., 19 (1) 35–47, 2022
https://doi.org/10.1007/s11998-021-00499-5

Operability limits for non-Newtonian liquids in dual-layer slot coating processes using the viscocapillary model

Jin Seok Park, Taehyung Yoo, Byoungjin Chun, Kwan-Young Lee, Hyun Wook Jung

Received: 21 December 2020 / Revised: 15 March 2021 / Accepted: 17 March 2021
© American Coatings Association 2021

Abstract The operability windows and coating bead dynamics for the dual-layer slot coating process with non-Newtonian coating liquids were investigated using the viscocapillary model, a two-dimensional (2D) CFD simulation, and experiments. The simplified viscocapillary model derived from the 2D equation of motion with the shear-thinning Carreau liquids bounds the uniform coating regime without defects such as leaking, bead break-up, and mid-gap invasion in dual-layer coating systems. The coating bead flows from experiments and finite-volume-based 2D simulations with the volume-of-fluid scheme demonstrate the performance of the viscocapillary model in reliably tracking the upstream meniscus position of the bottom layer in the coating bead region. The onset of leaking, bead break-up, and mid-gap invasion defects is strongly affected by the rheological properties of Carreau-type coating liquids and the flow ratio between the top and bottom layers. In particular, the relative thickness of the shear-thinning bottom layer at the onset of mid-gap invasion is smaller than the well-known 1/3 value in the Newtonian case, depending on the degree of shear thinning.

Keywords Dual-layer slot coating, Shear-thinning, Viscocapillary model, Mid-gap invasion, Operability limits

This paper was presented at the 2020 International Society of Coatings Science and Technology Conference that was held virtually September 20–23, 2020.

J. S. Park, T. Yoo, B. Chun, K.-Y. Lee,
H. W. Jung (✉)
Department of Chemical and Biological Engineering, Korea University, Seoul 02841, Republic of Korea
e-mail: hwjung@grtrkr.korea.ac.kr

Introduction

Slot coating is a versatile and favorable coating method that is importantly applied in various industrial applications, including lithium-ion secondary batteries, solar/fuel cells, flat display panels, and functional films.[1–4] As a premetered coating type, the final wet coating thickness is determined by the flow rate and the speed of the moving substrate or web only at a given coating width. Thus, such a slot coating feature allows the precise control of the final wet film thickness, regardless of the liquid properties, even at high production rates.[5–8]

Despite the simple premetered relation, the stable operation range of the process can be restricted by the flow conditions and die configuration in the coating bead region bounded by die lips, a moving substrate, and upstream/downstream menisci. Practically, the slot coating flow is reliably manipulated when the upstream meniscus in the coating bead is within both ends of the upstream die lip. This position can be approximately determined using a simplified model, i.e., the viscocapillary model. A certain limit, called the operability window, exists in the coating operation for guaranteeing the stable coating bead flow in the form of the flow rate versus the substrate speed (or bead pressure versus substrate speed).[9–11] There are two main types of coating defects, leaking (or weeping) and bead break-up, which are closely related to the upstream meniscus position. Leaking is typically observed under relatively high-flow-rate or low-web-speed conditions when the upstream meniscus position is pushed beyond the upstream die lip. In contrast, bead break-up, covering ribbing, rivulets, barring, and air entrainment, occurs when the upstream meniscus position approaches the slot feed. In this case, microvortices of air begin to form between the coating liquid and substrate as the flow rate further decreases (or the substrate speed increases).

In recent years, the industrial demand for dual-layer (or multilayer) slot coatings continues to increase for their time and energy saving aspects. However, research on dual-layer slot coating is not yet being actively conducted—despite the growing industrial role of this process—owing to the complex flow controls involved. For the dual-layer slot coating process, a simplified model for predicting the pressure gradient in the rectilinear-like coating bead regime was first introduced by Cohen.[12] Taylor and Hrymak[13] clarified the effect of the midstream die lip geometry on the shape of a liquid–liquid interface and vortex formation via flow visualization and finite element simulations. Nam and Carvalho performed systematic extensive studies on the stability of the liquid–liquid interface in the coating bead[14,15] and established vortex-free operating conditions for two-layer tensioned-web-over-slot die coating.[16] Ji et al.[17] presented a practical viscocapillary model for Newtonian dual-layer slot coating flow based on the model for single-layer coating and observed a good agreement between their experiments and 2D computational fluid dynamics (CFD) computations. Schmitt et al.[1] elaborately constructed operability windows of dual-layer slot coating with power-law liquids.

Another important aspect of the dual-layer slot coating method is the proper control of the interfacial stability in the coating bead region. As highlighted by Musson,[18] two layers in the coating bead can form an interface with no inter-diffusion owing to the corresponding extremely short residence time. The interface starts from the separation line located at the midstream die lip and is usually located at the downstream corner of the midstream die lip under stable conditions. A mid-gap invasion phenomenon inevitably occurs when the separation line between the top and bottom liquids migrates toward the upstream corner of the midstream die lip, as first presented by Nam and Carvalho.[14] They also addressed two possible modes for such separation line jumps depending on the viscosity ratio of the two coating liquids. The separation line gradually travels in the upstream direction when the bottom layer is more viscous. However, for the more viscous top layer, the microvortex under the midstream die lip grows, and the separation line abruptly jumps to the upstream-wise corner after the vortex touches the liquid–liquid interface. As another coating defect in which the recirculation or vortex under the midstream die lip significantly deteriorates the separation line, the onsets of mid-gap invasion in the non-Newtonian dual-layer slot coating are required to be further scrutinized in the operability limits.

A few studies have been conducted on dual-layer slot coating systems for non-Newtonian coating liquids. In this study, a simplified 1D viscocapillary model for non-Newtonian Carreau liquids in dual-layer slot coating processes was employed to predict the upstream meniscus position of the bottom layer and guide the practical operability windows (in the form of flow rate versus web speed under lab-scale experimental range). In addition, the conditions at which the mid-gap invasion between the non-Newtonian layers begins were newly marked on operability window maps. It is known, in the case of Newtonian dual-layer coating, that the mid-gap invasion is liable to occur when the ratio between the bottom-layer thickness and the coating gap becomes less than 1/3.[14] However, this simple indicative value for the mid-gap invasion onset is dependent on the shear-thinning nature of the layers, as is described in Results and discussion section. The simplified model for the shear-thinning layers was validated by comparing the operating windows predicted from 2D CFD simulations and experiments performed using a lab-scale slot coater. It was also confirmed that the pressure and velocity profiles in the coating bead region obtained from the model and the simulation agreed well with each other. The flow reversal under the midstream die lip was also observed as a direct evidence of mid-gap invasion from CFD simulation and viscocapillary model, as in Tusda[19] and Kwak and Nam,[20] where power-law fluids were considered. Furthermore, the effect of the liquid property and/or the flow ratio on the operability limits and mid-gap invasion was taken into consideration.

Viscocapillary model for non-Newtonian dual-slot coating flow

The viscocapillary model is a simple, but reasonable tool for identifying the operability of the slot coating process according to the position of the upstream meniscus under the given operating conditions, which can be derived from momentum balances inside the upstream and downstream coating bead regimes. This model is known to be reliable when the capillary number ($Ca = \eta U/\sigma$, which represents the relative effect of viscous drag to the surface tension force and where η, U, and σ represent the liquid viscosity, characteristic velocity, and surface tension, respectively) in the coating bead region is low,[8,21] where the momentum balance in the sub-regions is correlated with both the viscous and capillary contributions.

Figure 1a presents a schematic of the coating bead region for dual-layer coating with various notations. h_u, h_m, and h_d denote the upstream, midstream, and downstream coating gaps, respectively. L_u, L_m, and L_d are the upstream, midstream, and downstream die lip lengths, respectively. Their dimensional values are presented in Experimental methods section and Fig. 1b. The flow rates through the two feed slots are $Q_{in,1}$ and $Q_{in,2}$ for the bottom and top layers, respectively. Here, each flow rate and web speed U_{web} can be used to determine the wet thicknesses of the bottom ($h_{\infty,1}$) and top ($h_{\infty,2}$) layers. The upstream meniscus of the coating bead is bound by the upstream die lip and substrate, in which shape is determined by the surface tension exerted on the liquid. ϕ and θ represent the static and dynamic contact angles of the upstream

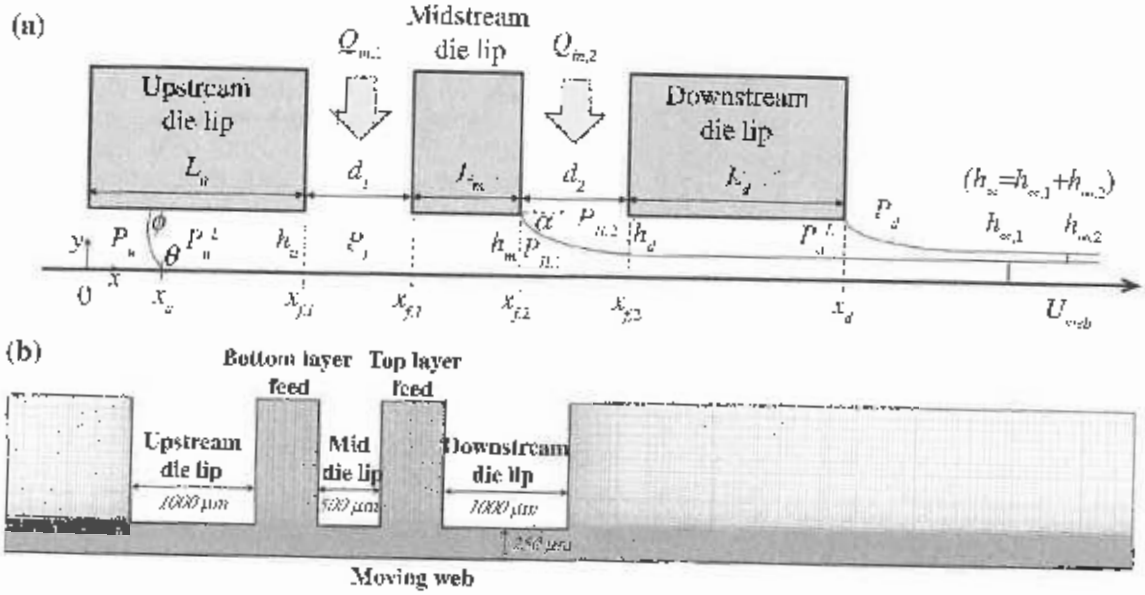

Figure 1: (a) Schematic and (b) computation grids of the coating bead region in dual-layer slot coating process

meniscus, respectively. Moreover, the liquid–liquid interface pinned to the downstream shoulder of the midstream die lip has a contact angle α. The x and y coordinates indicate the flow direction and coating gap direction, respectively.

Employing the lubrication approximation, the steady velocity profile along the coating gap can be obtained using the simplified x-component momentum equation (Eq. 1) for non-Newtonian liquids and the corresponding boundary conditions (Eq. 2). The Carreau liquid model with four parameters is adopted herein to feasibly portray the shear-thinning behaviors of coating liquids used in coating experiments.

$$0 = -\frac{\partial P}{\partial x} + \frac{\partial}{\partial y}\left(\eta(\dot{\gamma})\frac{\partial u_x}{\partial y}\right), \text{ where } \eta(\dot{\gamma}) = \eta_\infty + (\eta_0 - \eta_\infty)\left(1 + (\lambda\dot{\gamma})^2\right)^{\frac{n-1}{2}} \quad (1)$$

$$q_u = \int_0^{h_u} u_{x,1}\,\mathrm{d}y = 0 \text{ in the upstream die lip region} \quad (2a)$$

$$q_m = \int_0^{h_m} u_{x,1}\,\mathrm{d}y = U_{web}h_{\infty,1} \text{ in the midstream die lip region} \quad (2b)$$

$$q_d = \int_0^{h_{\infty,1}} u_{x,1}\,\mathrm{d}y + \int_{h_{\infty,1}}^{h_d} u_{x,2}\,\mathrm{d}y = U_{web}h_\infty \text{ in the downstream die lip region.} \quad (2c)$$

Here, u_x is the x-component velocity, P is the pressure, $\dot{\gamma}$ is the magnitude of shear rate ($|\partial u_x/\partial y|$), and η_0, η_∞, λ, and n represent the zero-shear viscosity, infinite-shear viscosity, relaxation time, and power-law index in the Carreau model, respectively. In addition, the bottom and top layers are denoted as subscripts 1 and 2, respectively. The velocity profiles below each die lip were separately solved using the two-step shooting method with a fourth-order Runge-Kutta scheme to simultaneously satisfy the flow rate per width conditions (Eq. 2), the no-slip boundary conditions (Eq. 3) in each die lip region, and the continuity conditions (Eq. 4) at the liquid-liquid interface in the downstream die lip region. Note that under a stable condition without the mid-gap invasion, a single liquid (i.e., bottom layer) flows basically in both upstream and mid-gap regions. However, since there are two liquid flows (i.e., top and bottom layers) in the downstream region, separate governing equations and continuity conditions (Eq. 4) for tangential stresses and velocities at the interface are required for each layer with different liquid properties. Here, the position of the liquid-liquid interface was assumed to be identical to the wet thickness of the bottom layer, $h_{\infty,1}$.

$$u_{x,1} = U_{web} \text{ at } y = 0 \text{ on the moving substrate} \quad (3a)$$

$$u_{x,1} = 0 \text{ at } y = h_u \text{ and } h_m,\ u_{x,2} = 0 \text{ at } y = h_d \text{ on the die lips} \quad (3b)$$

$$u_{x,1} = u_{x,2} \text{ at } y = h_{\infty,1} \text{ in the downstream die lip region} \quad (4a)$$

$$\eta_1(\dot{\gamma}_1)\dot{\gamma}_1 = \eta_2(\dot{\gamma}_2)\dot{\gamma}_2 \text{ at } y = h_{\infty,1} \text{ in the downstream die lip region.} \quad (4b)$$

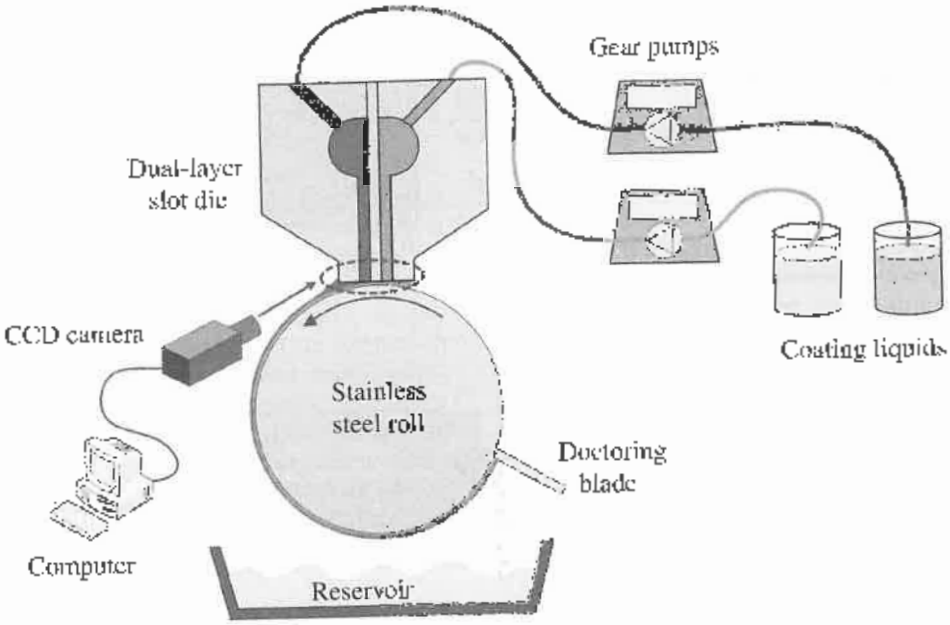

Figure 2: Schematic experimental setup of dual-layer slot coating process

The pressure differences ΔP_u, ΔP_m, and ΔP_d in the upstream, midstream, and downstream sub-regions, respectively, can be simply expressed as follows:

$$\Delta P_u = P_l - P_v^L = \nabla P_u(L_u - x_u),\ \Delta P_m = P_{\mathrm{II},1} - P_l - \nabla P_m L_m,\ \Delta P_d = P_d^L - P_{\mathrm{II},2} = \nabla P_d L_d. \tag{5}$$

Here, the pressure gradients ∇P_u, ∇P_m, and ∇P_d are determined numerically as mentioned above. The pressure differences over the three interfaces were simplified using the Young–Laplace relation as follows:

$$\Delta P_u^L = P_u^L - P_v = -(\cos\phi - \cos\theta)\frac{\sigma_1}{h_u} \tag{6a}$$

$$\Delta P_m^L = P_{\mathrm{II},2} - P_{\mathrm{II},1} = -(\cos\alpha - 1)\frac{\sigma_{\mathrm{II},1}}{h_d - h_{\infty,1}} \tag{6b}$$

$$\Delta P_d^L = P_d - P_d^L = 0.54\mathrm{Ca}_2^{1/2}\frac{\sigma_2}{h_\infty}. \tag{6c}$$

The shapes of the upstream meniscus (Eq. 6a) and liquid–liquid interface (Eq. 6b) were assumed to be an arc of a circle. Here, ϕ and θ were set as 60° and 120°, respectively, as in a previous study,[17,22] simply assuming the flat upstream meniscus by setting $\Delta P_u^L = 0$. The contact angle α between the top and bottom layers in the midstream region was obtained using $\cos\alpha = \left(d_2^2 - (h_d - h_{\infty,1})^2\right) / \left(d_2^2 + (h_d - h_{\infty,1})^2\right)$. As the physical properties of the top and bottom layers are typically similar in the majority of coating processes, the interfacial tension between the two layers $\sigma_{\mathrm{II},1}$ is assumed to be quite small, i.e., 0.001 N/m,[18] resulting in very minor pressure jump over the liquid–liquid interface. Furthermore, the curvature of the downstream free surface was approximated using the model proposed by Ruschak[23]—a modified version of Landau and Levich's[24]—which is valid in the capillary number range of $0.01 < \mathrm{Ca} < 0.1$ (Eq. 6c). Here, the apparent capillary number of the top layer is defined as $\mathrm{Ca}_2 = \eta_2(\dot{\gamma})U_{\mathrm{web}}/\sigma_2$, where $\eta_2(\dot{\gamma})$ and σ_2 are the shear viscosity at an effective shear rate and the surface tension of the top layer, respectively. The Ca range considered in this study was between 0.032 and 0.17.

After combining the pressure difference at each sub-region, the relation required to determine the upstream meniscus position x_u is presented as shown in Eq. (7). It should be noted that the bead pressure $\Delta P = P_d - P_u$ in Eq. (7) was set as zero herein for application to the experiments, i.e., P_d and P_u are both equal to the ambient pressure.

$$x_u = L_u - \frac{1}{\nabla P_u}\left[\Delta P - \Delta P_u^L - \Delta P_m^L - \Delta P_m - \Delta P_d - \Delta P_d^L\right]. \tag{7}$$

Experimental methods

A set of experiments was conducted using a laboratory-scale dual-layer slot coater to verify the viscocapillary model by visually constructing the operability limits. The position of the upstream meniscus was captured using a charge-coupled device (CCD) camera

as an indicator of leaking and bead break-up defects, where they lie at the far upstream and downstream ends, respectively, in the upstream die lip region. Figure 2 presents the schematic setup of a dual-layer slot coating experiment. A 5-cm-wide dual-slot die with two 500-μm feed slots (d_1 and d_2), 1000-μm upstream, 500-μm midstream, and 1000-μm downstream die lip lengths (L_{up}, L_{mi}, and L_{dn}, respectively) was installed along with a stainless-steel roll of 14.7-cm diameter. The coating gap between the die lips and roll surface ($h_g = h_{in} - h_d$) was set as 250 μm throughout the experiments. The web speed was varied from 0.1 to 12 m/min. Each coating liquid was fed to the top or bottom slot die from individual tanks using a gear pump (Cole-Parmer, EW-75211-35, USA) with a pump head (Cole-Parmer, EW-07002-25, and EW-73003-14, USA). Flow visualization via CCD camera (Prosilica, GX 1910C, Germany) with a light source (Moritex, MLEP-A035W31R, Japan) was used to track the upstream meniscus position and to determine the operability limits under flow rate and web speed variations. Here, experimentally observed onsets of the operability window were compared to those obtained with the viscocapillary model under three different total flow rate conditions (40, 60, and 80 mL/min). The flow ratio, which is defined as the ratio of the bottom layer thickness to the total wet thickness ($Q_R = h_{\infty,1}/h_\infty$), ranges between 0 (top layer only) and 1 (bottom layer only). The flow ratios of 0.4, 0.5, and 0.667 between the top and bottom layers were used in this study.

The fluid samples comprised mixtures of deionized (DI) water and glycerol (20:80 vol%) containing various contents of xanthan gum polymer. As xanthan gum is a highly hydrophilic biopolymer,[25] it was first dissolved in pure DI water using a homogenizer (Daihan, HT-50DX, South Korea). Then, subsequent to the addition of glycerol, the mixture was stirred for approximately 24 h using a magnetic bar in the vessel to ensure the complete mixing and appropriate degassing. Three types of coating solutions comprising various xanthan gum contents (0, 250, and 750 ppm) were produced and labeled as N, S1, and S2, respectively. The shear viscosities are plotted in Fig. 3, and the Carreau model parameters for application to the model and simulation are listed in Table 1.

CFD simulations

To determine the time-dependent 2D flow characteristics in the coating bead region and evaluate the performance of the viscocapillary model, a commercial CFD solver based on the finite volume method (FVM), i.e., Fluent (Ansys Inc., Fluent 17.0), was used in this study. Both the air–liquid and liquid–liquid interfaces were adjusted using the volume-of-fluid (VOF) scheme. Each phase in the computation cells is represented by a specific scalar transport function that

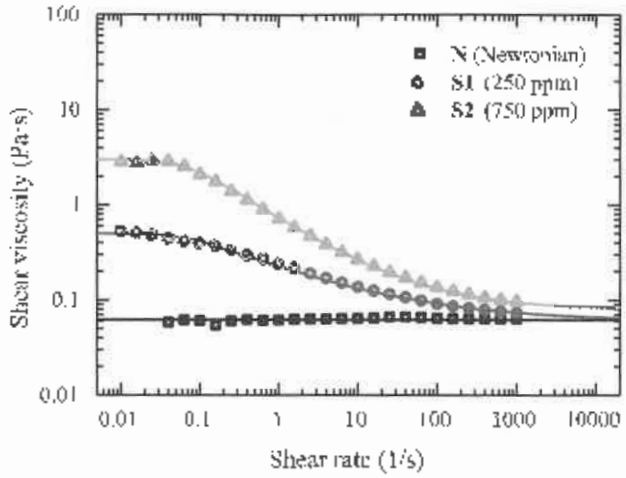

Figure 3: Shear viscosities of Newtonian (N) and shear-thinning (S1 and S2) coating liquids

ranges from 0 to 1. The operability limits were practically demarcated by the position of the static contact line of the upstream meniscus in the upstream die lip region.

Because the interface is distinguished from the interpolation of the scalar transport function of the VOF scheme, the accuracy of its position is directly proportional to the cell size in the computational domain. Moreover, a reduction in the cell size is also important for the feasibility of the viscocapillary motion of coating liquids within the coating bead. However, the use of many tiny cells may result in an excessive computational cost. The trade-off between numerical accuracy and computational cost was optimized through a mesh convergence test. The final mesh selected herein is shown in Fig. 1b with 50,950 cells, where the smaller cells are densely allocated in the coating bead region (200 elements in the x-direction of the longest die lip and 50 elements in the y-direction between the moving web and die lips).

In this simulation, the no-slip and no-penetration boundary conditions were imposed on the die lips and the moving web. The inlet velocities had a normal velocity profile, which satisfied the prescribed flow rate at each feed slot. The far upstream and downstream sides in the computational domain were set as pressure outlets of a specific value, i.e., atmospheric pressure. The physical properties of the top and bottom liquids are listed in Table 1. The static contact angle of the upstream meniscus was assigned to the value as in the viscocapillary model. However, the dynamic contact angle could not be assigned in the CFD simulation. Instead, the static contact angle between the liquid and moving web was iteratively specified to find the expected value of the dynamic contact angle (i.e., 120°), which was valid in low capillary coating bead flows.[7]

Table 1: Various material parameters and properties of coating liquids used in this study

Coating liquid		N	S1	S2
Carreau model parameters	Zero-shear viscosity η_0 (Pa s)	0.062	0.5	3.0
	Infinite-shear viscosity η_∞ (Pa s)	–	0.06	0.08
	Power-law index n (–)	–	0.64	0.45
	Relaxation time λ (s)	–	15	15
Surface tension σ (N/m)		0.064	0.062	0.060
Density ρ (kg/m^3)		1200	1200	1200

Results and discussion

Comparison of operability limits and coating bead dynamics

The simplified viscocapillary model was first validated by comparing the limits of leaking and bead break-up defects determined from CFD simulations and experiments. Figure 4a displays the operability windows in the dual-layer coating bead flows for two liquids. The bottom layer was varied using N, S1, and S2, while the top layer was only set as N under a flow ratio of $Q_R = 0.5$. Throughout this study, the double-layer set is simply designated as "BS2-TN," if the bottom layer is S2 and the top one is N. The solid lines denote the operability onsets, demarcating the leaking and bead break-up predicted by the model. The dashed lines represent the onsets of the mid-gap invasion and indicate that the region under this line falls into the mid-gap invasion state. The closed and open symbols indicate the onsets determined from the experiments and 2D CFD simulations, respectively.

First, the onsets predicted by the model match satisfactorily with those obtained in experiments and simulations, considering the low Ca and low Reynolds number ($0.032 < Ca < 0.17$, $0.080 < Re < 0.78$) operations in this study. Here, Re is the dimensionless quantity of inertial force to viscous force, defined as $Re = h_m U_{web} \rho / \eta$. As the bottom layer is changed from N to S2, the upstream meniscus moves toward the downstream direction, which implies that the operability limits shift slightly to the left in the map. This can be explained by the "suppression effect"[7] wherein a more viscous bottom layer (S2 rather than N) is pushed to a lesser extent by the top layer emanating from the feed. In other words, a more viscous top layer could hinder the momentum transfer of the bottom layer to a greater extent, such that the upstream meniscus of the bottom layer moves more toward the upstream direction. The other example is addressed in the subsequent part of this paper.

Nam and Carvalho[14] demonstrated that in a thin coating operation, the mid-gap invasion occurs initially when the velocity underneath the midstream die lip changes in the direction opposite to the moving substrate, when the pressure at the downstream corner

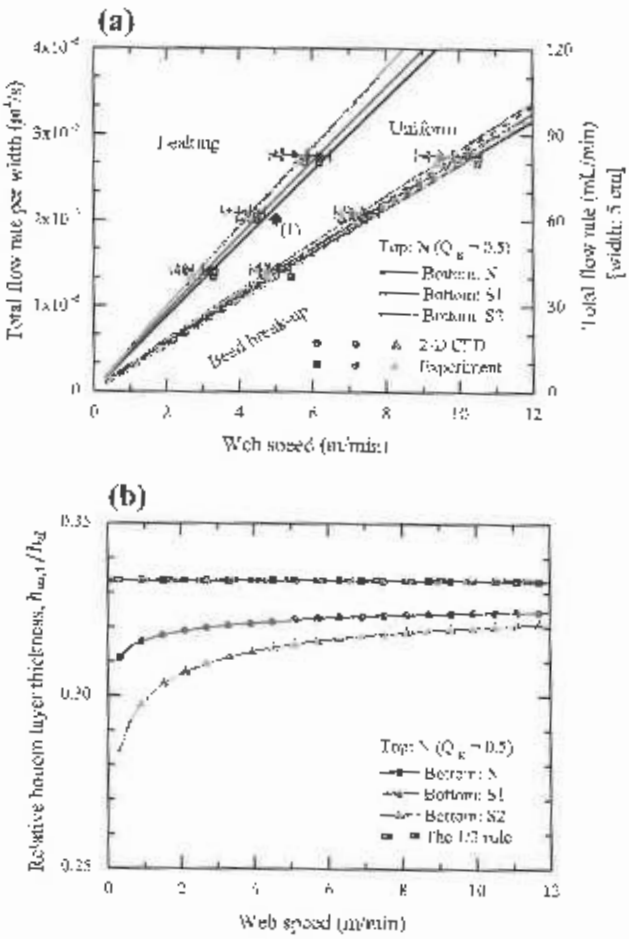

Figure 4: (a) Operability limits in the map of the total flow rate and web speed determined from the viscocapillary model, 2D CFD simulation, and experiments for dual-layer slot coating processes with various dual-layer sets (BN-TN, BS1-TN, and BS2-TN) and (b) the changes in onsets (critical bottom-layer thickness with respect to the coating gap) of mid-gap invasion along the web speed for the same dual-layer sets. The closed symbols in (a) are shifted slightly in the +y-direction for a better view

of midstream die lip is slightly higher than that at the upstream corner, i.e., the positive ΔP_{ny}. It is worth noting that they observed the simple and robust "1/3 rule" for the onset of mid-gap invasion in the Newto-

nian dual-layer slot coating process. That is, the mid-gap invasion is initiated when the wet thickness of the bottom layer is less than 1/3 of the coating gap (i.e., $h_{co,1}/h_d < 1/3$), which results in a flow reversal below the midstream die lip. The criterion value of $h_{co,1}/h_d$ was extended to shear-thinning systems by numerically finding a zero velocity gradient at the lip wall ($|\partial u_x/\partial y|_{y=h_m} = 0$) for the bottom layer in the midstream die lip under a given web speed. In Fig. 4b, onsets of the mid-gap invasion for three dual-layer sets (BN-TN, BS1-TN, and BS2-TN) in Fig. 4a, while varying the web speed, are presented. Compared to the Newtonian case (BN-TN), exactly corresponding to the simple 1/3 rule, the critical relative thickness of the bottom layer $h_{co,1}/h_d$ for the BS1-TN and BS2-TN cases decreases as the web speed decreases. In particular, the greater the shear thinning of the bottom layer, the lower the flow rate,[19,20] resulting in a smaller critical relative thickness, regardless of the viscosity level itself. This indicates that the onset of the mid-gap invasion is closely related to the viscosity variation along the coating gap at a given web speed in the midstream die lip region. Another example for a more shear-thinning bottom layer of low viscosity is presented subsequently.

A CCD camera was installed in the vicinity of the slot coater to capture the upstream meniscus and to obtain a side view of the coating bead flow state. As shown in Fig. 5, for the BS2-TN case, the experimentally observed and simulated upstream meniscus moved toward the feed position with an increase in the web speed from 3.7 and 4.0 m/min for the experiments and simulation, respectively, to 6.8 m/min under a fixed flow rate condition (q_{total}= 60 mL/min and $Q_R = 0.5$). The onsets of leaking (Fig. 5a, c) and bead break-up (Fig. 5b, d) exhibited a qualitatively good agreement with those obtained via the model. Note that Fig. 5d, which is obtained with the simulation near the bead break-up condition, shows slight oscillations of the total coating thickness and liquid–liquid interface, including unexpected air entrainment (This may be an artifact of the 2D CFD solver.).

The x-component velocity contours and profiles for the BS2-TN liquid set at three different locations inside the coating bead are presented in Fig. 6 under the operating conditions of $q_{total} = 60$ mL/min, $Q_R = 0.5$, and $U_{web} = 5$ m/min [i.e., point (1) in Fig. 4a]. The flow inside the coating bead comprises a combination of the Couette contribution owing to the moving web and the Poiseuille contribution induced by a pressure gradient. Therefore, the precise estimation of the pressure distribution is directly connected to the velocity profiles under the die lips. The velocity profiles obtained from the model and simulation in the coating gap direction at three locations are in good agreement with each other. In this case, mid-gap invasion may not occur because no flow reversal is observed under the midstream die lip (Fig. 6b).

As in the case of the dual-layer slot coating with two Newtonian liquids,[17] the pressure distributions along with the coating bead predicted in both the model and simulation were also compared for the above non-Newtonian dual-layer coating cases (BN-TN, BS1-TN, and BS2-TN) in Fig. 7 under the same operating conditions as those in Fig. 6. Although the pressure levels predicted from both methods are not exactly the same, the pressure gradients in the coating bead region are quite similar to each other, which actually affects the velocity profiles. It should be noted that the relatively lower pressure level around the midstream feeds from the model might be due to the lack of y-

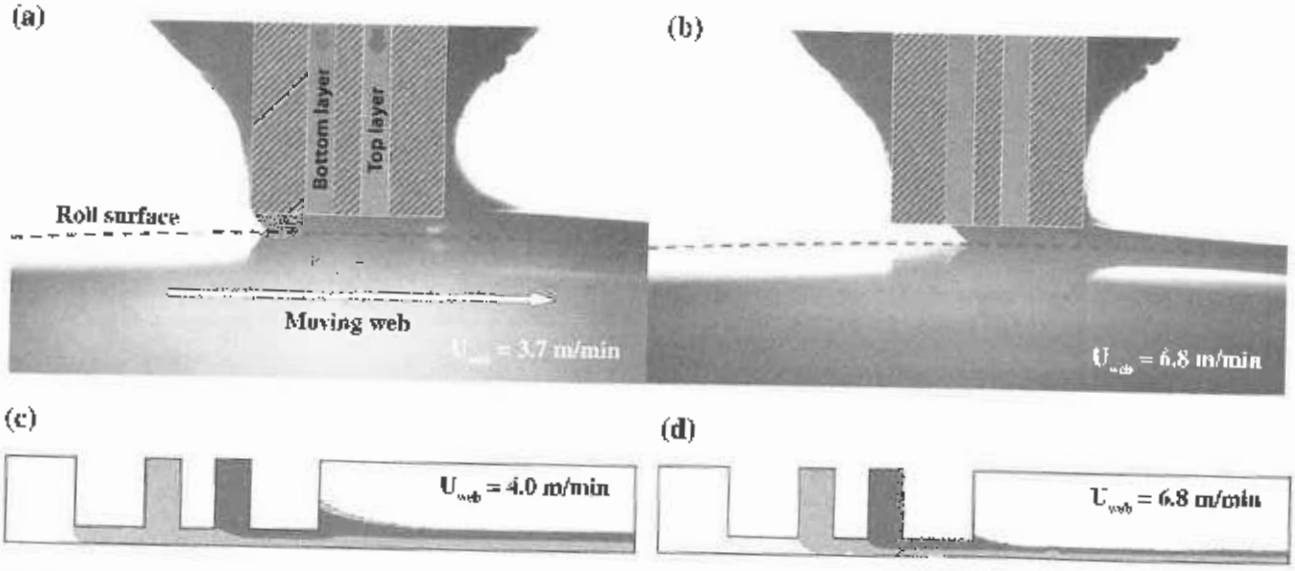

Figure 5: Visualization of the coating bead flows for BS2-TN liquids under a total flow rate of 60 mL/min and $Q_R = 0.5$. The web speeds used are (a) 3.7 m/min (near leaking) and (b) 6.8 m/min (near bead break-up) for the experiments and (c) 4.0 m/min and (d) 6.8 m/min for the CFD simulations

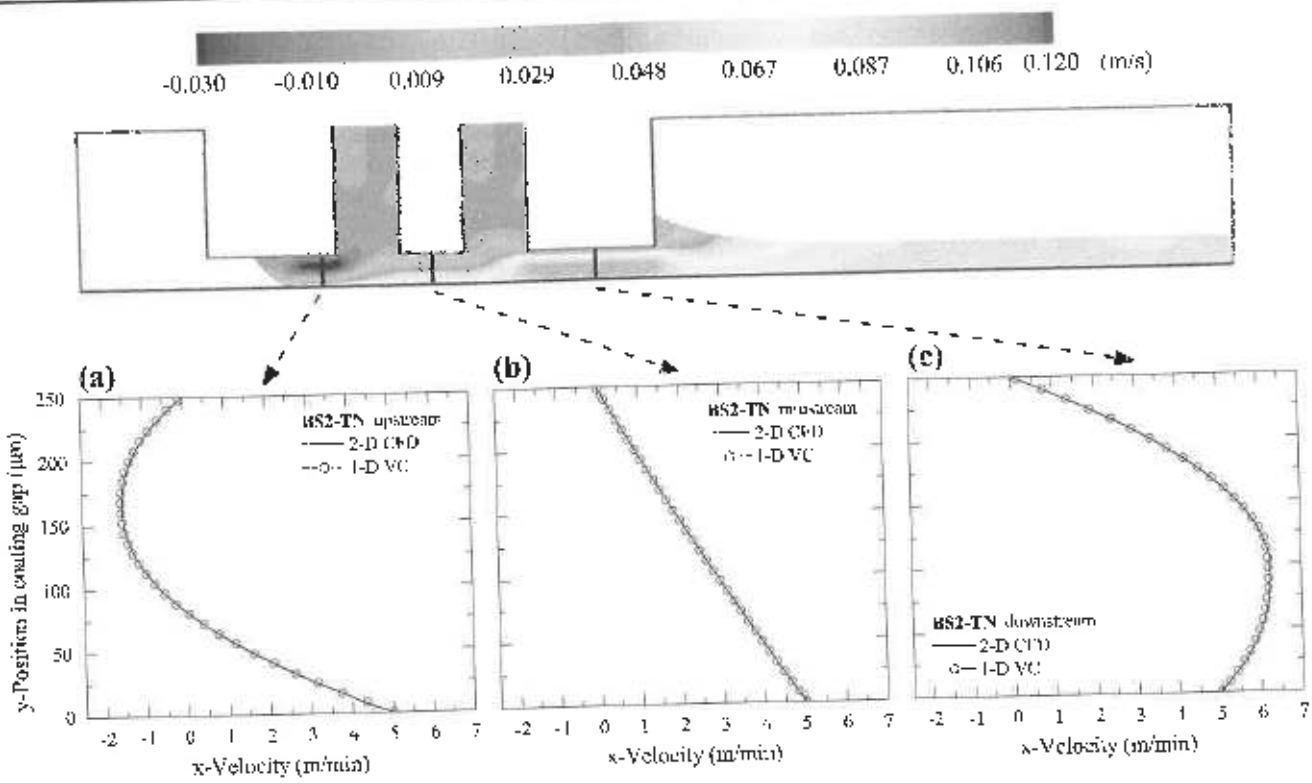

Figure 6: *x*-component velocity contour and local velocity profiles for BS2-TN liquid set as predicted from the model and simulation at (a) upstream, (b) midstream, and (c) downstream locations inside the coating bead region. The flow rate per width is 2×10^{-5} m²/s, $Q_R = 0.5$, and $U_{web} = 5$ m/min

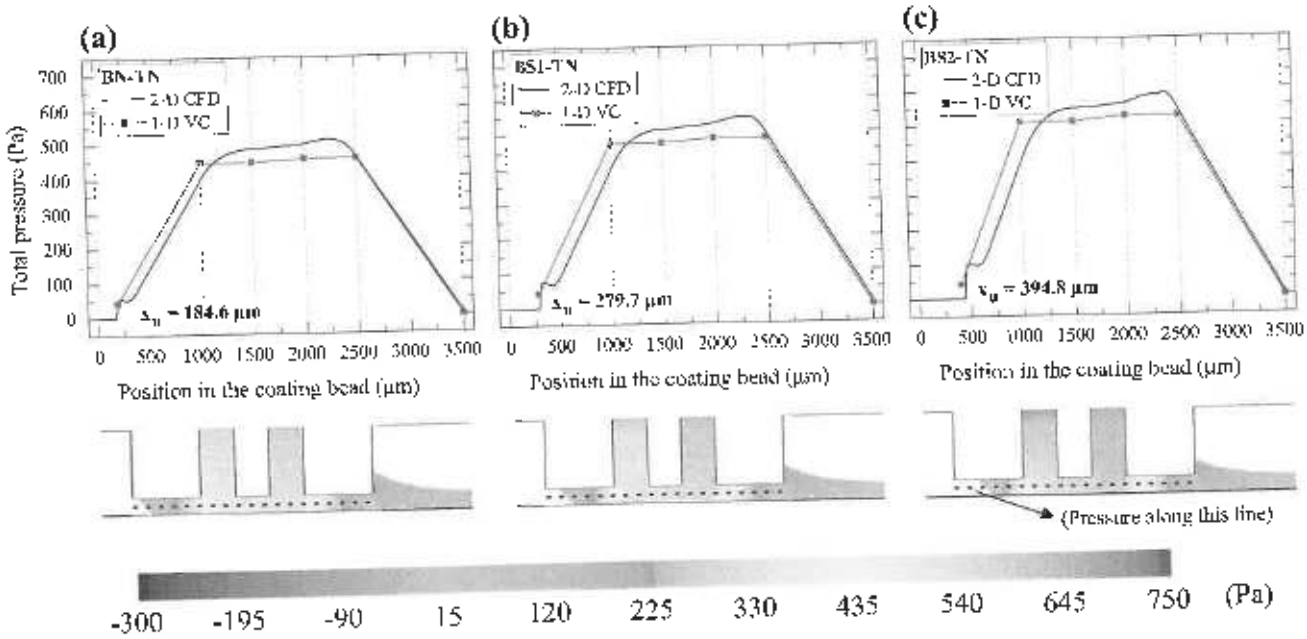

Figure 7: Pressure contours and distributions inside the coating bead region predicted from the model and simulation for (a) BN-TN, (b) BS1-TN, and (c) BS2-TN liquid sets. The flow rate per width is 2×10^{-5} m²/s, $Q_R = 0.5$, and $U_{web} = 5$ m/min

directional impact pressure information emanating from the feed flow, in contrast to the CFD simulation case. In addition, the positions of the upstream meniscus calculated via both methods coincided well with each other (the values shown in Fig. 7 were determined by the viscocapillary model), thus supporting the validity of the model.

Effect of the flow ratio on the operability limits

Figure 8a presents the change in the operability limits for the BS2-TN liquid set in dual-layer slot coating flows under various flow ratio conditions (Q_R = 0.4, 0.5, and 0.667). As the flow ratio decreases (the bottom layer becomes thinner), the momentum exerted near the upstream feed region decreases, thus resulting in the downstream-wise movement of the upstream meniscus. As a result, the operability window shifts toward the lower web speed direction (to the left). Moreover, the onset of the mid-gap invasion varies significantly. As the flow ratio decreases, the momentum of top layer with relative high flow rate at its feed becomes greater than that of the bottom layer, which induces the positive ΔP_{in} under the midstream die lip,

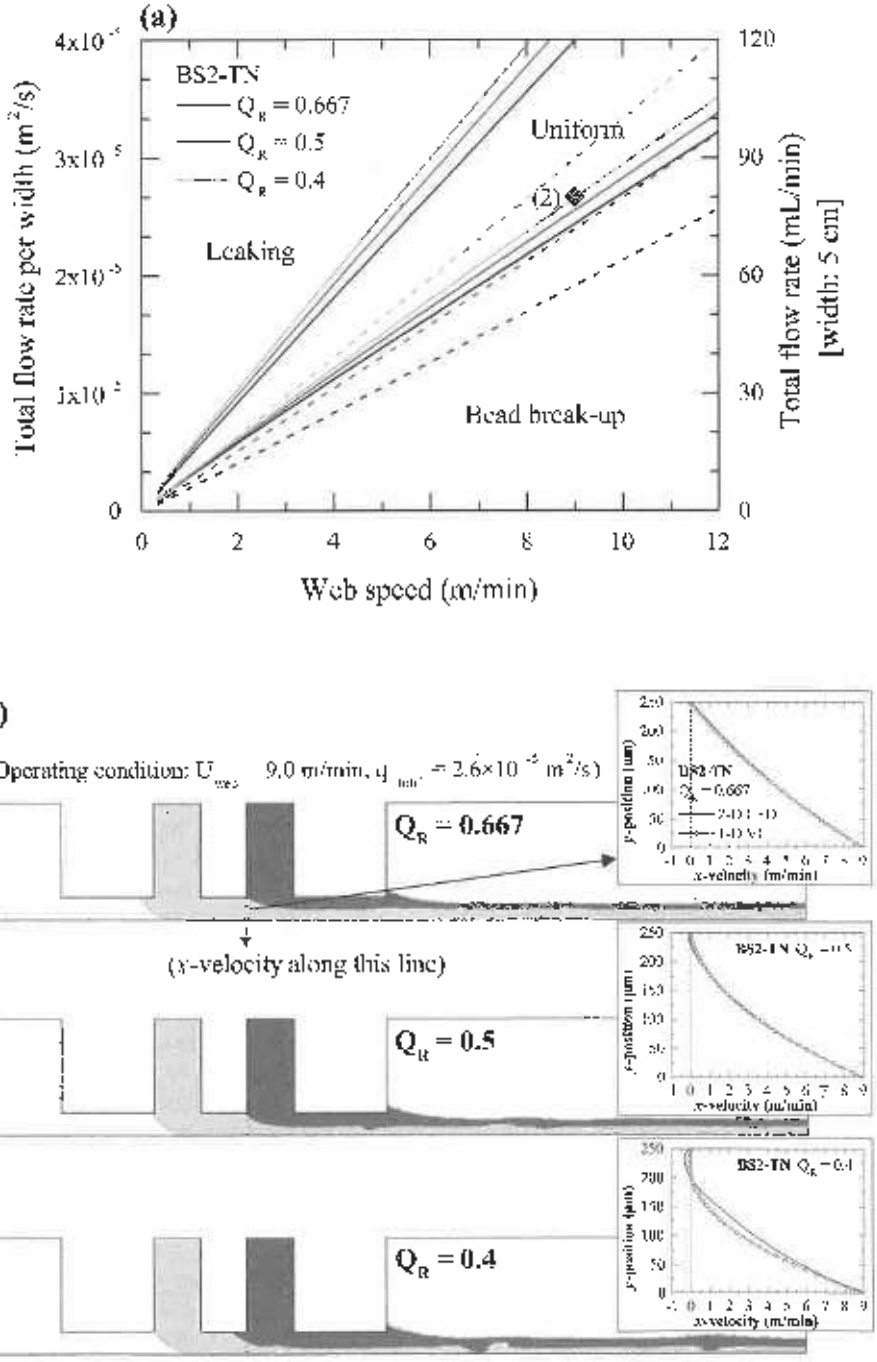

Figure 8: (a) Effect of the flow ratio of BS2-TN liquid set on operability window. (b) Coating bead flows obtained from 2D CFD simulations at point (2) in Fig. 8a under three flow ratio conditions (Q_R = 0.667, 0.5, and 0.4). The *x*-velocity profiles under midstream die lip are shown

and finally results in flow reversal. The corresponding coating bead flows and x-component velocity profile are displayed in Fig. 8b under the operating conditions indicated by point (2) in Fig. 8a ($U_{web} = 9$ m/min and $q_{total} = 80$ mL/min, or equivalently, $q_{total} = 2.6 \times 10^{-5}$ m^2/s). As the flow ratio decreases, it is prominent that the liquid-liquid interface moves toward the upstream direction. For example, the case wherein $Q_R = 0.4$ is beyond the onset of the mid-gap invasion, thus exhibiting flow reversal under the midstream die lip. Note that slight bead break-up phenomena including unstable liquid–liquid interfaces were observed for the cases of $Q_R = 0.5$ and 0.4. The x-velocity profiles showed a clear flow reversal in the mid-gap region for $Q_R = 0.4$ case due to the backward pressure action in the midstream, which is in the mid-gap invasion, as depicted in Fig. 8b. Albeit the good agreement of velocity profiles from 1D model and 2D simulation for $Q_R = 0.667$ and 0.5 cases, there is a slight difference in velocity profiles for $Q_R = 0.4$ case. This might be because the simple viscocapillary model could not predict the actual unstable flow features under the mid-gap invasion, although it usefully acts as a good indicator for determining defect-free operability regions.

Effect of rheological properties of coating liquids in the model

A model analysis was further performed to explore the effect of shear-thinning properties on the mid-gap invasion. As shown in Fig. 9a, Carreau liquids having various power-law indices and lower viscosity levels in comparison with the Newtonian liquid are arbitrarily selected (the parameters are listed in the legend). Their surface tension values are assumed to be the same as that of the Newtonian liquid N in Table 1. It is obvious from Figs. 4b and 9b that the onset of mid-gap invasion is much lower than that according to the 1/3 rule when

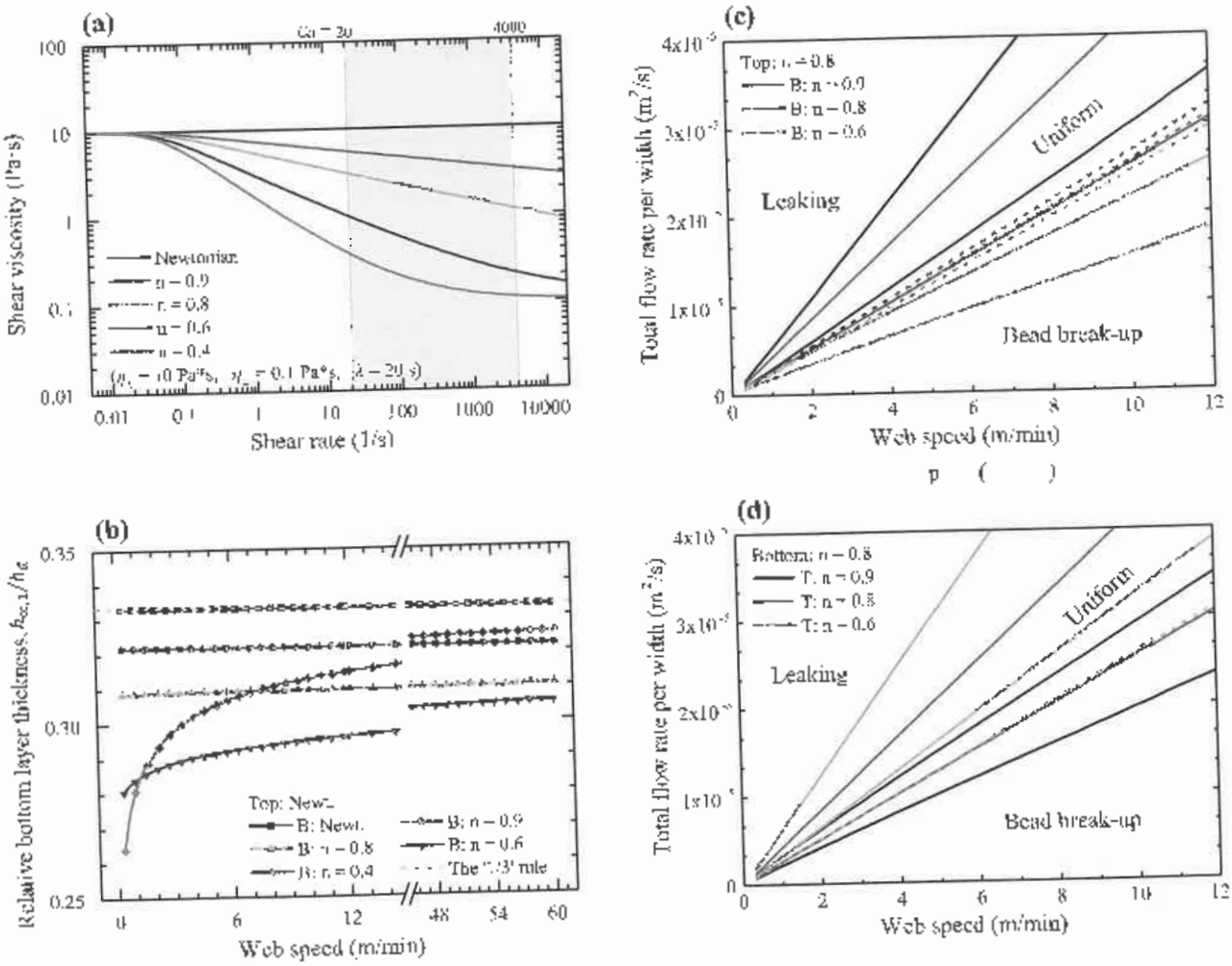

Figure 9: (a) Shear viscosities of various Carreau model liquids. (b) Onsets of mid-gap invasion as a function of the web speed for various dual-layer sets. (c) and (d) present the operability windows for various dual-layer model liquid sets when the bottom layer or the top layer is varied

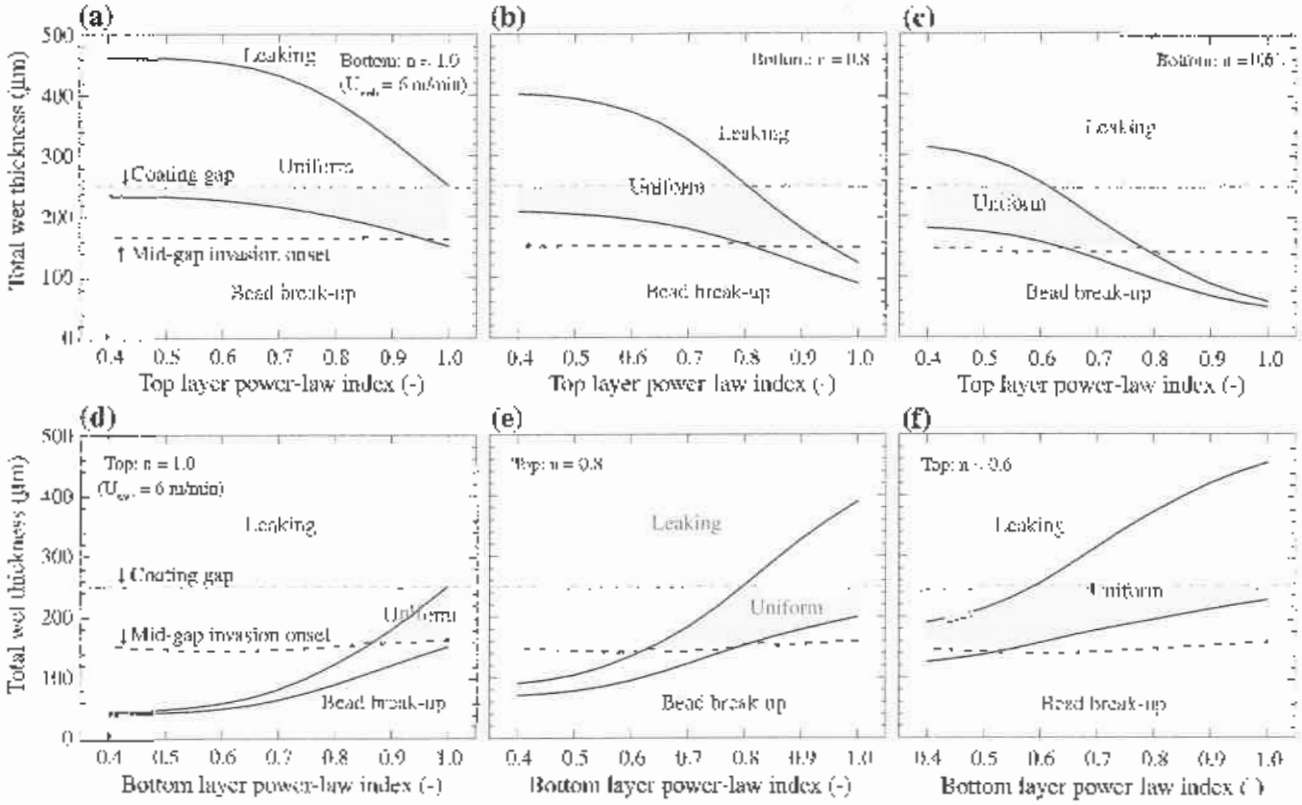

Figure 10: Various operating limits in terms of total wet film thickness with varying power-law index of coating fluids under U_{web} = 6 m/min. Effect of the degree of shear thinning of the top layer [(a)–(c)] and bottom layer [(d)–(f)]

the bottom layer becomes more shear thinning, regardless of the viscosity level, at the given operating conditions. Note that the bottom layer was varied, while the top layer was fixed as a shear-thinning liquid with n = 0.8 because the mid-gap invasion is mainly related to the bottom layer. The web speed was varied between 0.3 and 60 m/min, which corresponds to the effective shear rate (U_{web}/h_m) of 20–4,000 s^{-1} in the coating bead, as shown as shaded region in Fig. 9a. When the shear rate is low, i.e., ca. 20 s^{-1}, the onset of the mid-gap invasion decreases accordingly to the order of the power-law index. As the shear rate increases, however, this order can change depending on the rate at which the viscosity decreases. The relative bottom-layer thickness $h_{co,1}/h_d$ is inversely proportional to the rate of viscosity change (or degree of shear thinning) at the given shear rate. The degree of shear-thinning by power-law index n is directly related to the onset, as pointed out by Kwak and Nam,[20] for power-law fluids. For a bottom layer of n = 0.4, for instance, the steeper local viscosity slope at a low web speed results in a lower onset value, which is significant deviation from the 1/3 value. This onset value gradually approaches 1/3 as the local viscosity slope approaches zero as the web speed increases.

Figure 9c, d presents the operability windows for the different dual-layer sets to ascertain the effect of shear-thinning under constant flow ratio Q_R = 0.5. As shown in Figs. 4a and 9c, the power law index of the bottom layer is varied; however, the shifting of the operability windows with respect to n occurs in opposite directions. This behavior implies that the suppression effect[17] is linked with the magnitude of the viscosity and not the degree of shear thinning. For example, in Fig. 9c, as the degree of shear thinning of the bottom layer increases (lower power-law index n), the relative viscosity of the top layer increases. The more viscous top layer acts as a barrier to the momentum transfer of bottom layer, thus causing the upstream meniscus to move toward the upstream direction and accordingly the operability window to shift in the higher web speed direction. The same principle is applied when the top layer changes, as shown in Fig. 9d. Note that the onsets of mid-gap invasion in Fig. 9d are identical under the fixed bottom-layer condition.

Figure 10 presents a comparison of the operability windows for various top and bottom layers with the Carreau parameters presented in Fig. 9a under the constant flow ratio and web speed conditions (Q_R = 0.5 and U_{web} = 6 m/min). From Fig. 10a–c, as the n value of the top layer increases, the top layer becomes more viscous, thus acting as a suppression barrier, which results in a narrower uniform coating range with a thinner wet thickness. The opposite trend is observed in Fig. 10d–f; the increasing n value of the bottom layer, in comparison with the top layer case, results in a

wider uniform coating range with a thicker wet thickness. It should be noted that the mid-gap invasion onset values in Fig. 10d–f are not constant since the shear-thinning parameter of the bottom layer is changed. Considering the practical aspects of coating operation, the shaded area in Fig. 10 is further marked between length scales of the coating gap and the mid-gap invasion within the uniform wet thickness regime. If the top layer is much less viscous than the bottom layer (when the power-law index of the top layer is less than that of the bottom layer here), the higher wet thickness corresponding to the leaking onset than the coating gap is predicted by the model. A simple and reliable operability window setup for non-Newtonian dual-layer coatings using the simplified viscocapillary model would be useful in coating industries that deal with multilayer functional films.

Conclusions

The operability windows and coating bead dynamics for the dual-layer slot coating process with non-Newtonian coating liquids were explored via the viscocapillary model derived from the lubrication approximation of 2D governing equations. The coating limits including leaking, bead break-up, and mid-gap invasion in the coating bead region have been reasonably predicted from the model, exhibiting a good agreement along with experiments and FVM-based 2D simulations. The effects of the shear-thinning properties of Carreau-like coating liquids and the flow ratio between the top and bottom layers were systematically investigated. The mid-gap invasion defect, which affects the formation of a uniform interface between the layers, was newly established in the operability windows for non-Newtonian shear-thinning liquids. The results revealed that the critical relative thicknesses of the mid-gap invasion for shear-thinning layers were less than 1/3 in the Newtonian case, depending on the degree of shear thinning at a given operating condition. Furthermore, the onsets of leaking and bead break-up defects for shear-thinning liquids were dominantly influenced by the viscosity level of each layer during a certain coating operation. This model can be usefully applied as a simple and reliable tool for determining the operability limits in dual-layer slot coating systems for non-Newtonian coating liquids.

Acknowledgements This research was supported by the National Research Foundation of Korea (NRF) of Korea Grant (2016R1A5A1009592) and the Ministry of Trade, Industry & Energy (MOTIE, Korea), under the Industrial Technology Innovation Program (No. 20011712).

References

1. Schmitt, M, Raupp, S, Wagner, D, Scharfer, P, Schabel, W, "Analytical Determination of Process Windows for Bilayer Slot Die Coating," *J. Coat. Technol. Res.*, **12** 877–887 (2015)
2. Diehm, R, Weinmann, H, Kornberg, J, Schmitt, M, Fleischer, J, Scharfer, P, Schabel, W, "Edge Formation in High-speed Intermittent Slot-Die Coating of Disruptively Stacked Thick Battery Electrodes," *Energy Technol.*, **8** 1–8 (2020)
3. Parsekian, AW, Harris, TAL, "Scalable, Alternating Narrow Stripes of Polyvinyl Alcohol Support and Unmodified PEDOT:PSS with Maintained Conductivity Using a Single-Step Slot Die Coating Approach," *ACS Appl. Mater. Interfaces*, **12** 3736–3745 (2020)
4. Kim, D-J, Shin, H-I, Ko, E-H, Kim, K-H, Kim, T-W, Kim, H-K, "Roll-to-roll Slot-die Coating of 400 mm Wide, Flexible, Transparent Ag Nanowire Films for Flexible Touch Screen Panels," *Sci. Rep.*, **6** 34322 (2016)
5. Sartor, L, "Slot Coating: Fluid Mechanics and Die Design," Ph.D. Thesis, University of Minnesota, Minneapolis, United States, 1990
6. Gutoff, EB, Cohen, ED, *Coating and Drying Defects: Troubleshooting Operating Problems*, 2nd edn. John Wiley & Sons, Hoboken, NJ (2006)
7. Kistler, SF, Schweizer, PM, *Liquid Film Coating: Scientific Principles and Their Technological Implications*. Springer, Berlin (1997)
8. Ding, X, Liu, J, Harris, TAL, "A Review of the Operating Limits in Slot Die Coating Processes," *AIChE J.*, **62** 2508–2524 (2016)
9. Higgins, BG, Scriven, LE, "Capillary Pressure and Viscous Pressure Drop Set Bounds on Coating Bead Operability," *Chem. Eng. Sci.*, **35** 673–682 (1979)
10. Lee, YW, Ahn, W-G, Nam, J, Jung, HW, Hyun, JC, "Operability Windows in Viscoelastic Slot Coating Flows Using a Simplified Viscoelastic-capillary Model," *Rheol. Acta*, **56** 707–717 (2017)
11. Ahn, W-G, Lee, SH, Nam, J, Kim, SJ, Lee, KY, Jung, HW, "Effect of Upstream Meniscus Shape on Dynamic Wetting and Operating Limits of Newtonian Coating Liquids in Slot Coating Bead Flows," *J. Coat. Technol. Res.*, **15** 1067–1076 (2018)
12. Cohen, D, "Two-layer Slot Coating: Flow Visualization and Modeling," MS Thesis, University of Minnesota, Minneapolis, United States (1993)
13. Taylor, SD, Hrymak, AN, "Visualization and Flow Simulation of a Two-layer Slot Coater," *Chem. Eng. Sci.*, **54** 909–918 (1999)
14. Nam, J, Carvalho, MS, "Mid gap Invasion in Two-layer Slot Coating," *J. Fluid Mech.*, **631** 397–417 (2009)
15. Nam, J, Carvalho, MS, "Linear Stability Analysis of Two-layer Rectilinear Flow in Slot Coating," *AIChE J.*, **56** 2503–2512 (2010)
16. Nam, J, Carvalho, MS, "Two-layer Tensioned-web-over-slot Die Coating: Effect of Operating Conditions on Coating Window," *Chem. Eng. Sci.*, **65** 4065–4079 (2010)
17. Ji, HS, Ahn, W-G, Kwon, I, Nam, J, Jung, HW, "Operability Coating Window of Dual-layer Slot Coating Process Using Viscocapillary Model," *Chem. Eng. Sci.*, **143** 122–129 (2016)
18. Musson, LC, "Two-layer Slot Coating," Ph.D. Thesis, University of Minnesota, Minneapolis, United States (2001)
19. Tsuda, T, "Coating Flows of Power-law Non-Newtonian Fluids in Slot Coating," *Nihon Reoroji Gakkaishi*, **38** 223–230 (2010)

20. Kwak, H, Nam, J, "Simple Criterion for Vortex Formation in the Channel Flow of Power-law Fluids." *J. Non-Newton. Fluid Mech.*, **284** 104372 (2020)
21. Weinstein, SJ, Ruschak, KJ, "Coating Flows." *Annu. Rev. Fluid Mech.*, **36** 29–53 (2004)
22. Gates, ID, "Slot Coating Flows: Feasibility, Quality." Ph.D. Thesis, University of Minnesota, Minneapolis, United States (1999)
23. Ruschak, KJ, "Boundary Conditions at a Liquid/Air Interface in Lubrication Flows." *J. Fluid Mech.*, **119** 107–120 (1982)
24. Landau, L, Levich, B, "Dragging of a Liquid by a Moving Plate." *Acta Physiochim. URSS*, **17** 141–153 (1942)
25. Phillips, GO, Williams, PA, *Handbook of Hydrocolloids*, 2nd edn. CRC Press, Boca Raton, FL (2009)

Publisher's Note Springer Nature remains neutral with regard to jurisdictional claims in published maps and institutional affiliations.